Mono-excitonic lasing of colloidal semiconductor nanocrystals in polymeric parabolic microcavities

Charlie Kersuzan, Sergei Celaj, Antony Nghanga, Céline Byl, Xiangzhen Xu, Willy Daney de Marcillac, Agnès Maitre, Thomas Pons

Mono-excitonic lasing of colloidal semiconductor nanocrystals in polymeric parabolic microcavities

Charlie Kersuzan,[1,2] Sergei Celaj,[2] Antony Nghangha,[1] Céline Roux-Byl,[1] Xiangzhen Xu,[1] Willy Daney de Marcillac,[2] Agneѕ Maître[2,*] and Thomas Pons[1,*]

[1] Laboratoire de Physique et d'Etude des Matériaux, ESPCI Paris, PSL University, CNRS, Sorbonne Université, UMR 8213, 10, rue Vauquelin, 75005 Paris, France

[2] Institut des Nanosciences de Paris, CNRS, Sorbonne Université, UMR 7588, 4, place Jussieu, 75005 Paris, France

Corresponding authors: agnes.maitre@insp.upmc.fr, thomas.pons@espci.fr

Abstract

Colloidal semiconductor nanocrystals constitute materials of choice to realize microlasers, thanks to the fine control of their optical and electronic properties, and to their solution processability. However so far, lasing has mostly been obtained under high excitation, in the biexciton regime. Here, we demonstrate instead that, in high-quality cavities, lasing naturally occurs in the single exciton regime. We describe the facile fabrication of nanocrystal-coated polymeric microcavities and study their lasing characteristics. We show that the lasing threshold lies in the sub-monoexcitonic excitation regime for CdS/CdSe/CdS quantum shells in particular, thanks to the high quality factor of the cavities and high transition cross sections of the quantum shells. We explain these results using a comprehensive model of nanocrystal optical properties. The model correctly reproduces lasing characteristics near and above the threshold. In this regime, in contrast to previous studies, the performance of the microlasers relies mostly on the transition cross section and the Stokes shift, not on biexciton recombination or exciton-biexciton splitting. This improved understanding will enable rational design of colloidal nanocrystals for low-threshold lasing applications.

Keywords: semiconductor nanocrystals, quantum dots, quantum shells, nanoplatelets, laser, optical gain, microcavities

Colloidal semiconductor nanocrystals are attractive materials for optical gain, thanks to their brightness, photostability and low lasing thresholds, their inexpensive colloidal synthesis and easy solution processability. In particular, they could facilitate miniaturization and integration into microphotonic devices thanks to the realization of microlasers.[1–5] Their electronic and optical properties can be tuned easily by varying their size and shape, thanks to quantum confinement, and by forming heterostructures such as core-shell nanocrystals. The synthesis of II-VI colloidal heterostructures based on CdSe is particularly well developed, including quantum dots (QD), nanoplatelets (NPL) and quantum shells (QS), all of which have demonstrated optical gain.[6,7,2,8–12] Band edge properties of QDs and QSs are usually represented with three electronic levels, with a ground state 0, a mono-excitonic state X, and a bi-excitonic state XX. In terms of optical gain, a simple atomic-like model predicts that 0 is absorbing, X is optically transparent and XX enables stimulated emission and optical gain.[3] In this description, lasing therefore relies on the biexcitonic state. This suffers from the rapid Auger relaxation in core-only QDs. However, Auger recombination is slowed down in CdSe/CdS core/shell nanocrystals thanks to the electron delocalization in the whole heterostructure. This has enabled demonstrations of low threshold biexcitonic stimulated emission and lasing using optical pumping or more recently using electrical pumping. [13]

Monoexcitonic lasing is more difficult to achieve due to the degeneracy of the system in this description. It has been demonstrated in special cases,[14] including charged QDs,[15–17] where this degeneracy is lifted by populating the first conduction band level with one extra electron, and type II QDs where it is lifted by large exciton-biexciton splitting due to Coulomb interactions.[18,19] Despite these realizations, there is a lack of general framework to describe optical gain in semiconductor nanocrystals and optimize their design.

Here, we compared QDs, QSs and NPLs and their ability to perform amplified spontaneous emission (ASE) in solution. We rationalize the effect of nanocrystal concentration and absorption cross-section on the ASE

threshold with a simple model. We then fabricated high quality factor polymeric microcavities by a simple photolithography technique and coated them with the different nanocrystals to study their lasing characteristics. We show that, in optimized systems, lasing originates from monoexcitons, not biexcitons, and start well below XX-X or X-0 population inversion. We propose a refined photophysical model to explain these and previous observations, introducing the Stokes shift between absorption and emission spectra as a crucial parameter for mono-excitonic lasing.

Results and discussion

Amplified stimulated emission in solution. We prepared different heterostructured nanocrystals based on CdSe and CdS. In these systems, valence band holes are confined in CdSe while the conduction band electrons are delocalized in both CdSe and CdS. This slows down Auger recombination, and thus favors radiative recombination of the biexciton and facilitates lasing. We prepared seven CdSe/CdS nano-heterostructures with three different geometries and different sizes: CdSe/CdS QDs[6,20–23] (QD-1, 2), CdS/CdSe/CdS QSs[11,12,24–26] (QS-1, 2, 3) and CdSe/CdZnS NPLs[8,10,27] (NPL-1,2; in these NPLs the shell is composed of an CdS-ZnS gradient alloy ranging from Cd-rich for the inner layers to Zn-rich in the outer layers). Dimensions, emission wavelengths, absorption cross sections, monoexciton and biexciton photoluminescence quantum yields of each nanocrystal type are presented in Tables S1-S3 in the Supporting Information. Average emission quantum yields are all in the 45-60% range for monoexcitons and in the 17-29% range for biexcitons.

These nanocrystals are often considered separately, and rarely compared under identical preparation and optical conditions. We have compared the ability of these different types of nanocrystals to perform amplified stimulated emission (ASE) under identical preparation and optical conditions.[1] In order to eliminate extrinsic factors which play key roles in ASE measured in close-packed films, such as variation of film thicknesses and scattering by surface rugosity, we measure ASE in solution for each sample, and

systematically vary the concentration of nanocrystals. We excited solutions of nanocrystals with a pulsed 532 nm laser line and collected the emission spectra in the direction of the line. As shown in Figure 1a,b, at low excitation intensity, the emission spectrum shows the Gaussian shape typical of monoexcitonic spontaneous emission. Above a threshold, a sharper emission line appears in the spectrum at wavelengths that are systematically blue-shifted with respect to monoexcitonic emission. This is consistent with the general experimental observations from the literature, in which gain is maximal at the wavelength of biexciton emission, and biexcitonic emission is blue-shifted compared to monoexcitonic emission in these CdSe/CdS heterostructures due to Coulomb repulsion. Assuming purely electronic transitions, the optical gain values associated with the XX-X and X-0 transitions are proportional to $\Delta N_i \, \sigma_{em,i}$, where ΔN_i is the population inversion between the corresponding XX-X and X-0 levels and $\sigma_{em,i}$ is the corresponding stimulated emission cross-section. Two simple arguments may then be used to explain the higher gain at the biexciton wavelength: (i) in QD and QS, the stimulated emission cross sections of the XX-X transition are twice those of the X-0 transition, due to the electronic level degeneracy; (ii) the XX-X population inversion reaches higher levels than the X-0 population inversion. Indeed, let's consider the population of the different levels as a function of excitation pulse energy expressed in $\overline{N}_{ph}$, the average number of photons absorbed per pulse, immediately after the end of the excitation pulse (Supporting Information discussion and Figure S5). As $\overline{N}_{ph}$ increases, $\Delta N_{X-0} = e^{-\overline{N}_{ph}}(\overline{N}_{ph} - 1)$ becomes positive for $\overline{N}_{ph} > 1$. However, this X-0 population inversion reaches a maximum of $e^{-2} \approx 0.13$ when $\overline{N}_{ph} = 2$, and then decreases for higher $\overline{N}_{ph}$, due to the progressive population of the XX level at the expense of the X population. In contrast, ΔN_{XX-X} can reach values close to 1 for high excitation pulse energy. Due to these two contributions, the maximal gain of the X-0 transition is about 15 times lower than that of the XX-X transition. In addition, if there is a spectral overlap between these transitions, this difference is further amplified, due to the competition of X-0 stimulated emission and X-XX reabsorption at lower $\overline{N}_{ph}$.

We then repeated this measurement for different concentrations. We observed that the ASE threshold systematically decreases as the concentration increases (Figure 1c). There is a minimal concentration, C_{min}, below which no ASE signal could be observed and above which the ASE threshold intensity decreases abruptly. This can be understood by considering that, below or near the threshold, the detected signal starts with a spontaneous emission event, emitted within the illuminated volume. The emitted photons are then either transmitted directly to the detector within a solid angle Ω_{coll}, or are transmitted through the illuminated solution within a much smaller volume Ω_{ASE}~S/L^2, where S and L are the section and length of illuminated solution volume. Depending on the population inversion, these can be either reabsorbed by other nanocrystals or elicit stimulated emission. Assuming a homogeneous illumination, and limiting our discussion to the blue-shifted XX-X transition observed experimentally, the total detected intensity at the end of the line, I, depends on the intensity emitted spontaneously per unit volume of solution, I_{sp}, the concentration C_{NC}, the population inversion, ΔN_{XX-X}, and the line length L , as:

$$I \sim I_{sp}\Omega_{coll} + I_{sp}\Omega_{ASE}\int_0^L e^{\Delta N_{XX-X}\sigma_{em,XX}C_{NC}\,z}dz \quad ,(1)$$

At low excitation power ($\Delta N_{XX-X} \ll 1$) the second term is negligible compared to the first one. Since $\Omega_{ASE} \ll \Omega_{coll}$, the ASE becomes detectable when the exponent becomes comparable to 1, that is, $C_{NC}\sigma_{em,XX}\Delta N_{XX-X}\,L \approx 1$. At most, $\Delta N_{XX-X} = 1$, which explains the existence of minimal concentration to obtain detectable ASE, $C_{min} \approx (\sigma_{em,XX}L)^{-1}$ (Supporting Information Figure S8). As shown in Figure 1d, we find indeed a clear correlation between C_{min} and σ_0, the absorption cross section at the central wavelength of the band edge excitonic transition (σ_0 is proportional to σ_{XX}, but not as the same wavelength). Above C_{min}, the range of measurable concentrations is limited by the solubility limit of nanocrystals, which vary depending of particle size and ligand coverage. Similarly to ASE, when using these nanocrystals within microcavities, we expect that reaching the lasing threshold will be facilitated

when $\sigma_{em,XX}$ is large. NPLs and QSs, with their high absorption cross-section at the band edge exciton transition, therefore seem to present more favorable photophysical properties.

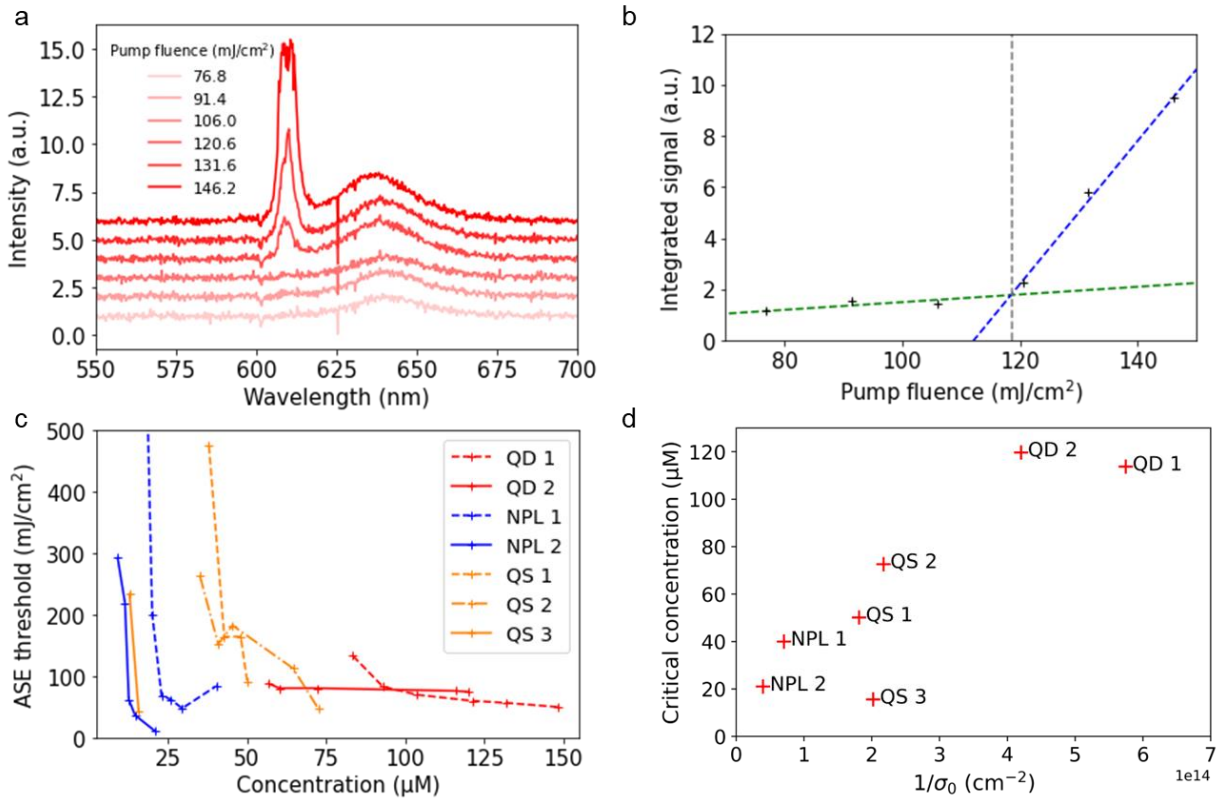

Figure 1 a. Photoluminescence spectra of a solution of QS collected in the direction of the excitation line, for different pump fluence; b. Integrated photoluminescence intensity as a function of the pump fluence. c: ASE pump fluence thresholds as a function of nanocrystal concentration for QD, QS, and NPL samples; d: Experimental minimum concentration required to observe ASE for the different samples, as a function of the inverse of the cross-section of their 0-X transition.

Fabrication of parabolic polymeric microcavities. In order to fabricate high quality factor microcavities, we used a modification of a recently reported photolithographic method.[28] A diluted SU8 photosensitive resin was spread as a thin film by spin coating, and illuminated by a Gaussian laser beam at 405 nm at the desired positions for controlled durations. The amount of deposited energy controls the diameter of the photo-crosslinked regions, since a local minimal energy deposition is required to perform cross-linking, as previously demonstrated. After baking and washing steps, these fabrication steps yield cylindrical

microdisks with vertical walls, presenting high quality whispering gallery modes.[28] However these modes are spread over the whole height of the microdisk and are susceptible to leaking into the underlying substrate. In order to improve confinement of the modes, we introduced a controlled amount of Tinuvin Carboprotect, a UV molecular absorber.[29] As a consequence, the local energy density deposited by the 405 nm laser beam, W, decreases with the lateral distance to the center, r, and with the penetration depth in the SU8 layer as:

$$\mathrm{W}(r,z) = 2\,\frac{P_0\tau}{\pi w_0^2}\,e^{-\frac{2r^2}{\mathrm{w}_0^2}}\,e^{-\epsilon_{405}C_{abs}(z_0-z)}, \quad (2)$$

where P_0 is the laser power, w_0 the beam waist, ϵ_{405} and C_{abs} the molar absorption coefficient at 405 nm of the absorber and its concentration in the film, z_0 is the film thickness and z is the coordinate along the height. Writing W_{c-l} as the cross-linking threshold, this results in a parabolic shape with a profile

$$z(r) = z_0 + \frac{2r^2}{\epsilon_{405}C_{abs}w_0^2} + \ln\left(W_{c-l}\frac{\pi w_0^2}{2P_0\tau}\right), \quad (3)$$

as shown in Figure 2a. When increasing the concentration of absorber in the film, Eq. (3) predicts that the walls curvature increases, as shown in Figure 2b. Scanning electron microscopy of microdisks realized with absorber concentrations of 10, 20 and 40 wt% shows that the shape indeed evolves accordingly and is retained after baking steps (Figures 2c, d). When labeled with QDs at a small concentration, the emission spectra of the QDs showed efficient coupling to whispering gallery modes, with high contrast and narrow (spectrometer resolution limited) peaks on top of the broader envelope (Figure S7). This suggests that these microcavities present a high quality factor (Q > 6,000), thanks to decoupling from the substrate and a smooth surface limiting scattering losses, as well as a high Purcell factor corresponding to an efficient coupling of the QD emission into the cavity modes.

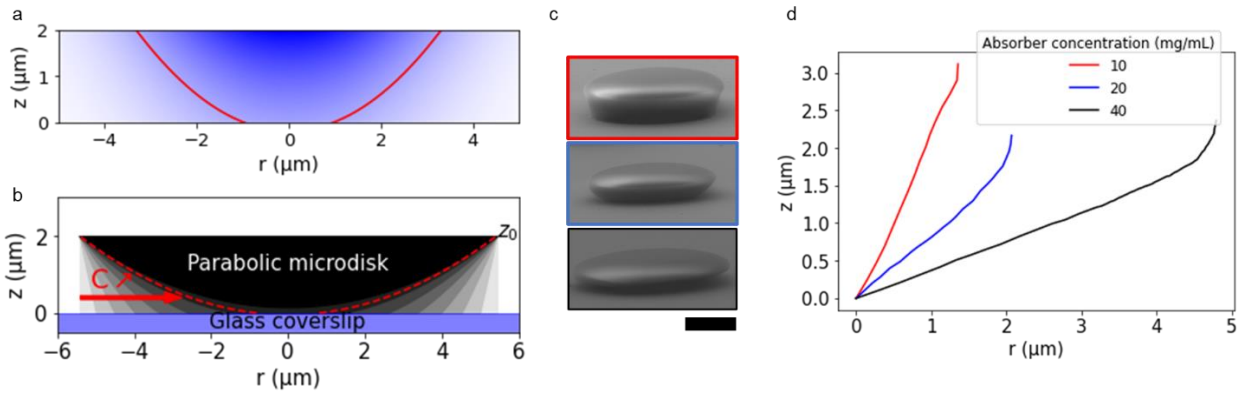

Figure 2 a: Laser intensity profile during photolithography as a function of the distance to the center and penetration depth into the resin film containing a UV absorber. The red line represents an iso-intensity profile, corresponding to a potential photo-crosslinking threshold as noted in Equation (3); b: Theoretical variations of the microdisk shape as a function of UV absorber concentration for similar laser irradiation conditions; c: Scanning electron microscopy of microdisks realized with 10, 20 and 40 mg/mL of UV absorber (Scale bar = 5 µm); d: Edge profiles of the same microdisks.

Nanocrystal lasing. We fabricated a series of parabolic microdisks with diameters in the range of 10 to 30 µm, and covered them with nanocrystals by spin coating. We excited the nanocrystals using a pulsed 532 nm laser from the top and collected the emission from the side (see Supporting Information). At low excitation intensity, the emission spectrum showed the broad envelope corresponding to spontaneous monoexcitonic emission. After a certain threshold, a narrow (< 0.2 nm FWHM) lasing peak appears (Figures 3a,b). These microcavities support whispering gallery modes separated by a few nm in wavelength.[30] Assuming that all these modes have similar quality factors, near the threshold, the nanocrystals start lasing in the mode where gain first exceeds cavity losses. Above this threshold, we observed lasing in the same mode, with instrument-limited spectral width (Figures 3c,d). Interestingly, all the QSs and NPLs samples exhibited lasing on the red side of their spontaneous emission spectra, in contrast to ASE or biexciton lasing which always occurs on the blue side.

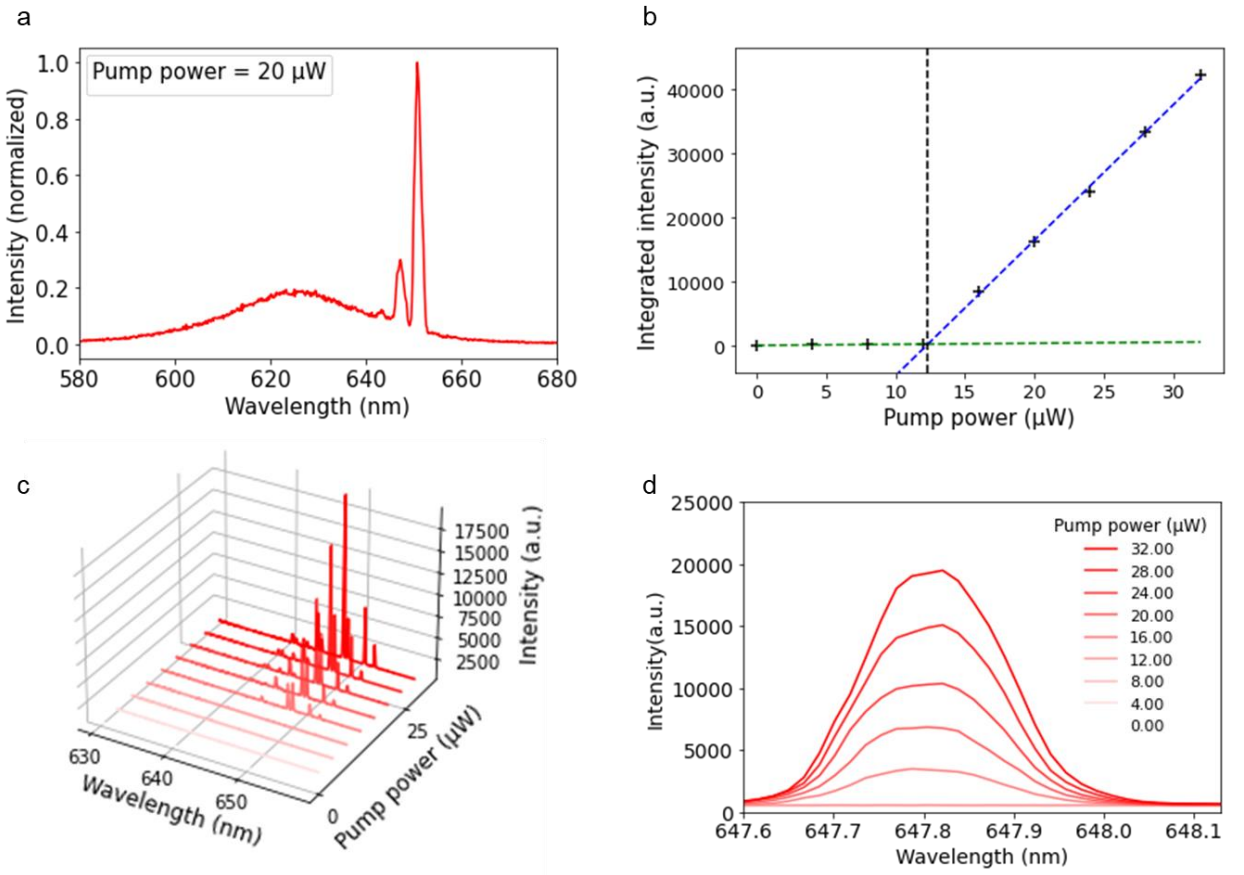

Figure 3 a: Typical emission spectrum of a microcavity coated with QS; b: Integrated intensity as a function of pump power; c: Series of photoluminescence spectra as a function of pump power; d: Spectrum of a lasing peak, for different pump power.

Model of nanocrystal gain. To understand this behavior, we propose a new model taking into account a key ingredient of photophysical properties of these nanocrystals which has so far remained neglected in lasing studies, which is the Stokes shift, Δ_S, between the absorption and emission spectrum maxima of the 0-X transition. In general, this shift originates from two sources: the fine structure of the exciton and the coupling to phonons.[31] In our cubic CdSe/CdS nanocrystals, the exciton fine structure splitting vanishes with increasing shell thickness due to the reduced electron-hole spatial overlap and absence of crystal field splitting.[32] However, the Stokes shift increases with shell thickness. This can be explained by an increased phonon coupling due to the increased charge separation, which has been previously observed

from the broadening of single particle emission spectra.[33,34] Taking this Stokes shift, Δ_S, into account requires considering 0, X and XX not as pure electronic states, but as an ensemble of vibrational sublevels (Figure S8). Only the lowest vibrational sublevels of 0, X and XX are significantly populated due to fast intraband relaxation. However, these sublevels absorb and emit photons into higher lying sublevels of 0, X and XX.

A complete description of the model is discussed in the Supporting Information, and we will only present the main arguments here. When considering stimulated emission, the relation between Einstein coefficients indicates that the stimulated emission cross-section spectrum is proportional to the spontaneous emission spectrum from the X state to the 0 state, ie. $B_{X-0}(\lambda) \propto A_{X-0}(\lambda)$. Furthermore, the symmetry between absorption and stimulated emission processes dictates that the amplitudes of the corresponding cross-sections are equal. For the 0-X transition, this leads to the following relation between the absorption cross-section, $\sigma_{abs,0}$ and the stimulated emission cross-section, $\sigma_{em,X}$:

$$\sigma_0(\lambda) \equiv \sigma_{abs,0}(\lambda) \approx\ 2\,\sigma_{em,X}(\lambda + \Delta_S), \quad (4)$$

where the factor 2 originates from the degeneracy of the 0 and X levels. When applying the same principles to the X-XX transition, we introduce an additional term Δ_{X-XX} corresponding to the X-XX splitting. We can therefore express the lineic optical gain of the nanocrystal medium, $g(\lambda)$, as:

$$g(\lambda) = C_{NC} \cdot (-\sigma_{high}(\lambda) - \sigma_0(\lambda)N_0 - \frac{1}{2}\sigma_0(\lambda + \Delta_{X-XX})N_X + \frac{1}{2}\,\sigma_0(\lambda - \Delta_S)N_X$$
$$+ \sigma_0(\lambda - \Delta_S + \Delta_{X-XX})N_{XX}) \ , \quad (5)$$

where $\sigma_{high}(\lambda)$ takes into account the absorption transitions occurring from states lying lower in the valence band and higher in the conduction band, C_{NC} is the nanocrystal concentration in the cavity and N_i are the population fractions of the *i* = 0, X and XX states. Below and at the threshold, the population fractions at the end of the excitation pulse can be derived as a function of the pump power, or equivalently,

of the average number of photons absorbed per nanocrystal per pulse, $\overline{N}_{ph}$. Figures 4a,b show the spectrum of lineic gain for different values of $\overline{N}_{ph}$ at the end of the excitation pulse. For emission wavelengths on the longer wavelength side of the X-0 spontaneous emission spectrum, the gain becomes positive at low pump power, for $\overline{N}_{ph} < 1$, but is limited in amplitude. On the other hand, for wavelengths closer to the XX-X emission spectrum, the lineic gain becomes positive only for larger $\overline{N}_{ph}$, but reaches much higher values. This is consistent with ASE experiments, where the concentration C_{NC} is small, and ASE can be observed only when the lineic gain is large enough, ie. near the biexciton emission wavelength. In agreement with our model, when C_{NC} increases, the ASE threshold occurs at lower excitation power. Since the ASE spectrum occurs at the wavelength of peak lineic gain at this excitation power, the ASE spectrum shifts to longer wavelengths at higher concentrations (see Figure S10-S12 and discussion in the Supporting Information).

In a microcavity, lasing starts in the mode where the lineic gain becomes equal to the lineic loss: $g(\lambda) = \Gamma_{loss}(\lambda) = \frac{2\pi cn}{\lambda Q}$, where *n* is the refractive index of the cavity and *Q* is the quality factor. At low excitation power ($\overline{N}_{ph} < 1$), the lineic gain is negative (absorption dominated) for shorter wavelengths but becomes positive (dominated by stimulated emission) for longer wavelengths. This behavior can be attributed to the Stokes shift, as discussed in the Supporting Information (Figure S13). As a consequence, we can define a factor of merit of the cavity and the nanocrystal medium as $K = \lambda Q\ C_{NC}\sigma_0/2\pi n$. If $K >> 1$ (high quality cavities/high nanocrystal concentration), the lineic gain can overcome lineic losses at longer wavelengths, well below 0-X population inversion. As K decreases, lasing requires higher gain to compensate losses. This higher gain is only reached at higher excitation intensity and for shorter wavelengths, as shown in Figures 4c,d.

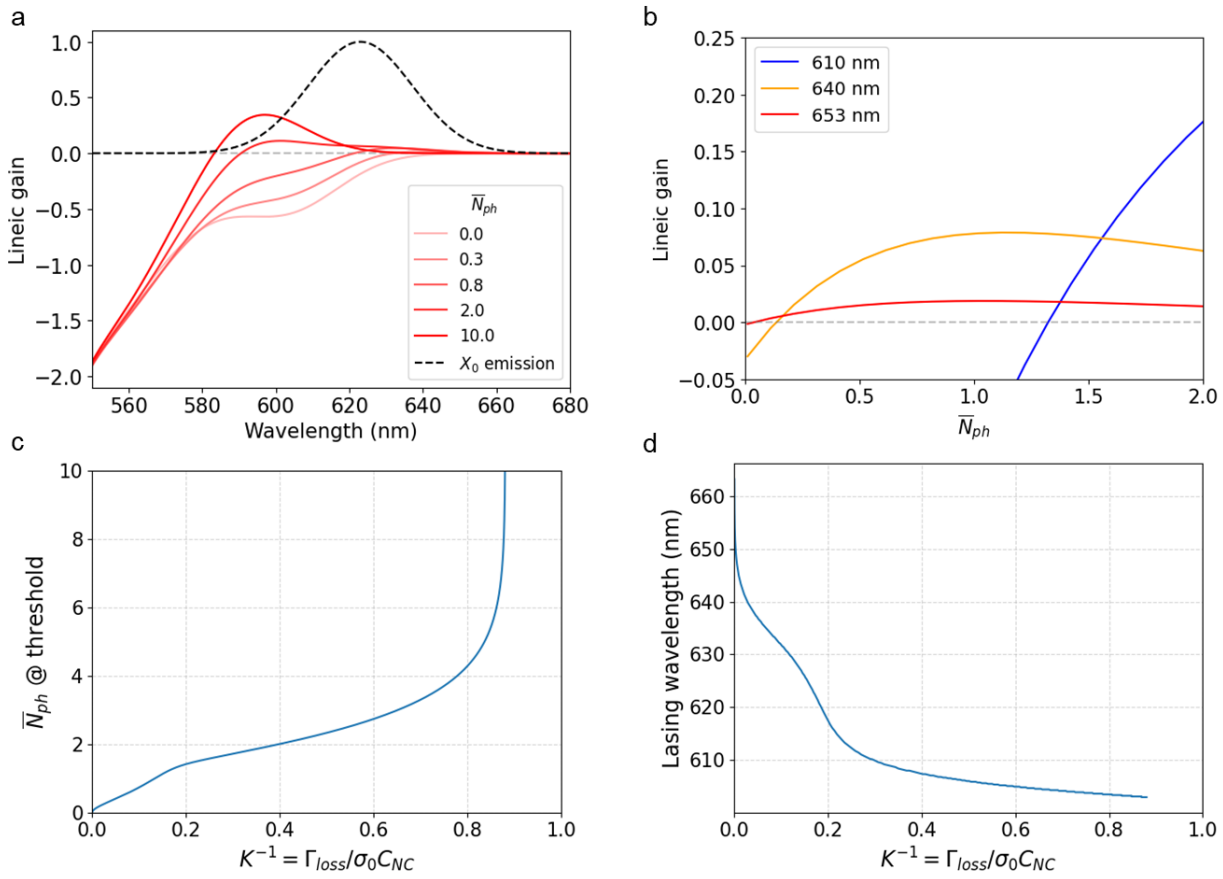

Figure 4 (a) Predicted spectrum of the lineic gain $g(\lambda)$ (normalized by $\sigma_0 C_{NC}$) as a function of the average number of photons absorbed per nanocrystal per pulse, $\overline{N}_{ph}$ for the QS-3 sample; (b) Variations of the normalized lineic gain at three different wavelengths as a function of $\overline{N}_{ph}$; (c) Evolution of $\overline{N}_{ph}$ at the lasing threshold as a function of K^{-1};(d) Predicted evolution of the lasing wavelength (ie. wavelength of maximal lineic gain) as a function of K^{-1}.

In summary, in our WGM microcavities where lasing is possible at a range of different wavelengths, the mode which starts to lase first should be redder with lower thresholds for higher K, and bluer with higher thresholds for lower K. In order to validate our model, we examined the lasing thresholds and wavelengths for 63 microcavities covered with quantum shells QS-3. Lasing thresholds are translated directly from pump power into $\overline{N}_{ph}$ (see Supporting Information). We then compared the values obtained with the model described above. As shown in Figures 5a,b, there is a clear correlation between lasing wavelengths and threshold excitation intensity which is consistent with our model. The vast majority (95 %) of the cavities studied display thresholds corresponding to an average number of photons absorbed per QD

below 0.5, where the contribution of the biexcitonic state is minimal. In a small percentage of cavities, the quality factor is lower, which may be due to film inhomogeneities or impurities in the photosensitive resin. This results in lasing thresholds which are much (up to 20 times) higher. These lower quality microcavities require larger lineic gain in order to lase, which occurs only in the biexcitonic state, and are characterized by a lasing wavelength which is blue-shifted compared to monoexcitonic spontaneous emission.

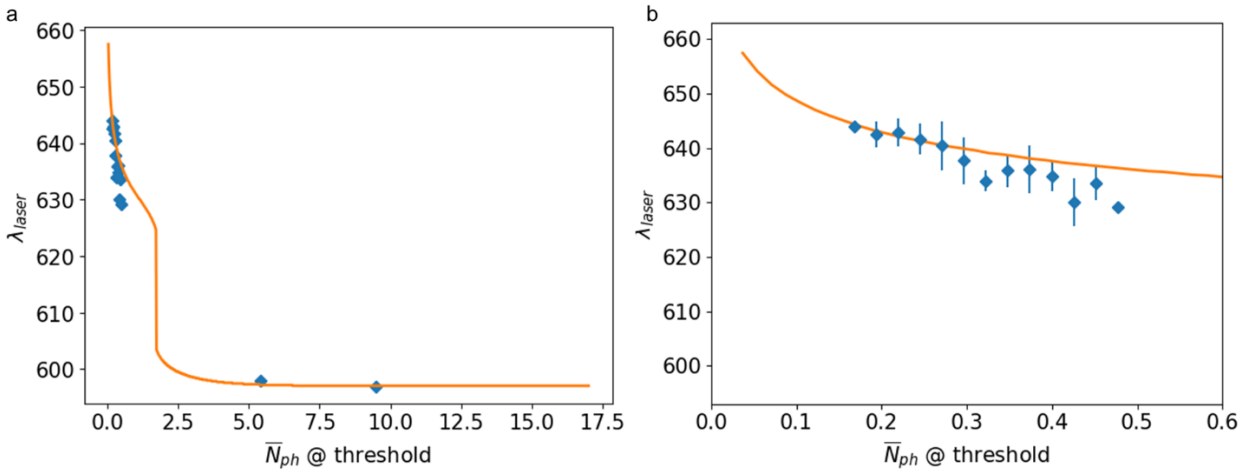

Figure 5. a: Experimental average lasing wavelengths as a function of the lasing threshold, expressed in $\overline{N}_{ph}$ units, for 63 microcavities covered with QS3 (diamonds) and values predicted by the model (line); b: Zoom on the low threshold region.

This behavior is general to QS and NPL samples, when spin-coated as solutions of similar optical density. We show the relationship between $\overline{N}_{ph}$ at the lasing threshold and the difference between the wavelengths of lasing, λ_{laser}, and central spontaneous emission, λ_0, measured for two QS samples (Figure 6a) and one NPL sample (Figure 6b). For QS samples, lasing threshold occurs mainly below $\overline{N}_{ph} < 0.5$, and at redshifts between 10 and 25 nm above λ_0. NPLs also follow the same behavior: NPL microcavities lasing at the lowest thresholds lase at redder wavelengths, between 10 and 25 nm above λ_0. The lasing wavelength then blueshifts towards λ_0 for microcavities with higher thresholds. For NPLs, $\overline{N}_{ph}$ could not directly derived experimentally due to the absence of variation in the spontaneous emission spectra with excitation power in our excitation range. However, the theoretical absorption cross-section at the

excitation wavelength provides a calculated $\overline{N}_{ph}$. The lowest thresholds lie above $\overline{N}_{ph} = 2$. This is consistent with the photophysical properties of NPLs, in which more than two excitons may coexist in the same nanoplatelet at the same energy, due to the large lateral dimensions of the NPLs.[35] As a consequence, the number of photons absorbed per NPL $\overline{N}_{ph}$ at the threshold needs to be higher, in order to reach the same level of population inversion $N_X - N_0$. None of the QD samples provided any observable lasing in our conditions. Compared to the QS and NPL samples, QDs possess lower σ_0 cross sections (Table S2). As a result, K may be too low to enable lasing. In addition, films of QDs showed more heterogeneities, which may decrease the quality factor and K, and prevent lasing. Optimizations of QD deposition conditions, together with the use of QDs with larger cores and σ_0 cross sections should however in principle also enable mono-excitonic lasing.

Finally, we examined the behavior of these microlasers above the threshold. Figure 6c shows the evolution of a QS microcavity emission spectrum as a function of the excitation power. As the excitation power increases above the threshold (here, $\overline{N}_{ph} \geq 0.3$), the mode which lases first remains dominant up to $\overline{N}_{ph} \approx 10$. In order to understand this behavior, we used a coupled differential equation model taking into account the same photophysical parameters as described above and the competition between pumping and stimulated emission during the excitation pulse (see Supporting Information). As shown in Figure 6d, predictions from this model correctly reproduce experimental observations. As the excitation power increases above the lasing threshold, photons populate the cavity mode faster and in higher numbers, and de-excitation of nanocrystals by stimulated emission can compensate the pump excitation. Therefore, lasing occurs at the same wavelength, even though excitation power is several times higher than the threshold. This more comprehensive model also correctly predicts the relationships between lasing wavelength, threshold, quality factor and nanocrystal concentration, (see Supporting Information and Figure S18-S19).

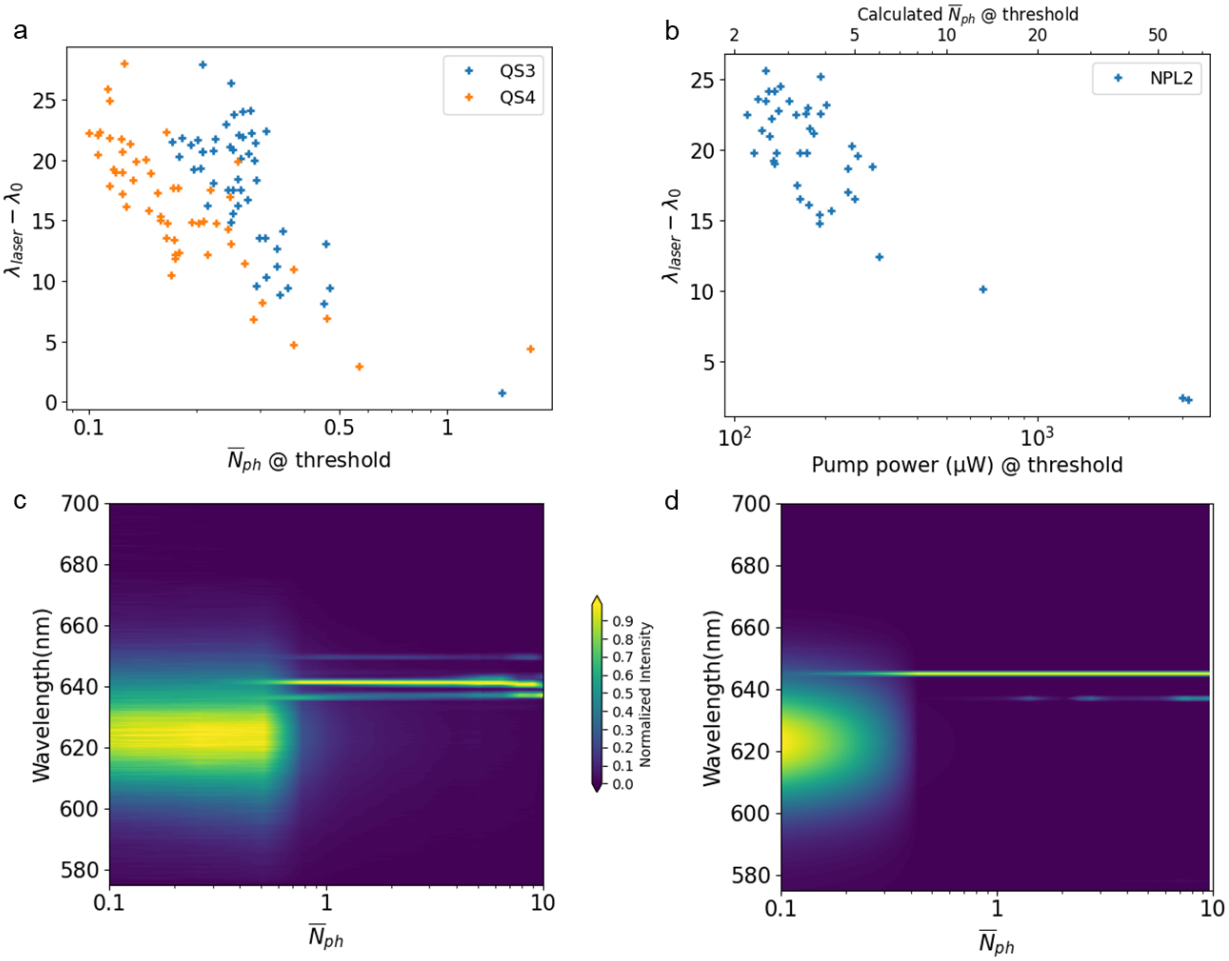

Figure 6. Comparison of the difference between the lasing wavelength, λ_{laser} , and the central wavelength of spontaneous emission, λ_0 as a function of lasing threshold for two QS samples (a) and NPLs (b). Experimental (c) and predicted (d) evolution of the emission spectrum of microcavities covered with QS3 as a function of pump power, expressed in $\overline{N}_{ph}$ units.

Conclusion

In conclusion, we have demonstrated the fabrication of parabolic microcavities using a simple photolithography method. The high quality of these cavities enables monoexcitonic lasing from different samples of nanocrystals. We propose a general model describing absorption and stimulated emission in nanocrystal medium, which reconciles the experimental observations from ASE experiments and cavity lasing from different samples and with reports from the literature. This also provides directions for further

optimization of nanocrystal design for more efficient lasing. At low quality factors, reducing Auger recombination rate is crucial to minimize losses and optimize bi-excitonic lasing. However, at high quality factors, mono-excitonic lasing is favored and the major parameters to optimize become the Stokes shift and the cross section of the 0-X transition.

Materials and Methods:

Nanocrystal synthesis. Nanocrystals were synthesized in hot non coordinating solvent using adaptations of previously described protocols, as detailed in the Supporting Information. [36,23,37,38,11]

Amplified stimulated emission in solution. Solutions of nanocrystals in toluene were loaded into 3 mm quartz cuvettes. A 20 Hz, pulsed doubled YAG laser at 532 nm is focused as a line into the solution. The emission is collected from the side, in the direction of the line, and focused into a multimode fiber connected to a spectrometer.

Microcavity fabrication. For the parabolic microdisks fabrication, SU8-2015 was diluted in cyclopentanone with a 3:2 SU8:cyclopentanone ratio. Tinuvin carboprotect was dissolved in the mix typically at a concentration of 20 mg/mL and used as a UV absorber. The lithographic process is then identical to the one from Ref. [28]. The deposition of titanium and gold layers was carried out under vacuum by thermal evaporation using a Vinci PVD-4E system. Modified SU8 was spin-coated onto the gold-coated coverslip. The resin was then soft-baked, exposed to a 405 nm cw laser (Oxxius) focused through a 10x, NA 0.3 microscope objective. A pattern of microdisks was realized by exposing the resist to the laser for typically 50 ms at 500 µW at a fixed position, before moving to the next position. A post-exposure bake step was then performed, followed by development and hard bake. Nanocrystals were spin-coated onto the microcavities as a solution in toluene. Experimental details are provided in the Supporting Information.

Spectroscopy of nanocrystal-coated microcavities. The microcavities were excited from the top by a 20 kHz laser at 532 nm focused through a 10x, 0.25 NA objective. The fluorescence spectrum was collected

from the side using a 50x, 0.55 NA objective and focused into a multimode fiber connected to a spectrometer.

Acknowledgements: The authors acknowledge funding from the Agence Nationale pour la Recherche (Nanowhispers, ANR-21-CE42-0029) and from the Institute of Materials Science (iMAT) of the Alliance Sorbonne Universite.

Supporting Information. Additional description of experimental protocols and modeling.

References:

(1) Klimov, V. I.; Mikhailovsky, A. A.; Xu, S.; Malko, A.; Hollingsworth, J. A.; Leatherdale, C. A.; Eisler, H.-J.; Bawendi, M. G. Optical Gain and Stimulated Emission in Nanocrystal Quantum Dots. *Science* **2000**, *290* (5490), 314–317. https://doi.org/10.1126/science.290.5490.314.

(2) Fan, F.; Voznyy, O.; Sabatini, R. P.; Bicanic, K. T.; Adachi, M. M.; McBride, J. R.; Reid, K. R.; Park, Y.-S.; Li, X.; Jain, A.; Quintero-Bermudez, R.; Saravanapavanantham, M.; Liu, M.; Korkusinski, M.; Hawrylak, P.; Klimov, V. I.; Rosenthal, S. J.; Hoogland, S.; Sargent, E. H. Continuous-Wave Lasing in Colloidal Quantum Dot Solids Enabled by Facet-Selective Epitaxy. *Nature* **2017**, *544* (7648), 75–79. https://doi.org/10.1038/nature21424.

(3) Park, Y.-S.; Roh, J.; Diroll, B. T.; Schaller, R. D.; Klimov, V. I. Colloidal Quantum Dot Lasers. *Nat. Rev. Mater.* **2021**, *6* (5), 382–401. https://doi.org/10.1038/s41578-020-00274-9.

(4) García de Arquer, F. P.; Talapin, D. V.; Klimov, V. I.; Arakawa, Y.; Bayer, M.; Sargent, E. H. Semiconductor Quantum Dots: Technological Progress and Future Challenges. *Science* **2021**, *373* (6555), eaaz8541. https://doi.org/10.1126/science.aaz8541.

(5) Li, H.; Zhao, Y.; Qiu, Y.; Gao, H.; He, K.; Yang, J.; Zhao, Y.; OuYang, G.; Ma, N.; Wei, X.; Du, Z.; Jiang, L.; Wu, Y. Multi-Interfacial Confined Assembly of Colloidal Quantum Dots Quasisuperlattice Microcavities for High-Resolution Full-Color Microlaser Arrays. *Advanced Materials* **2024**, *36* (23), 2314061. https://doi.org/10.1002/adma.202314061.

(6) García-Santamaría, F.; Chen, Y.; Vela, J.; Schaller, R. D.; Hollingsworth, J. A.; Klimov, V. I. Suppressed Auger Recombination in "Giant" Nanocrystals Boosts Optical Gain Performance. *Nano Lett.* **2009**, *9* (10), 3482–3488. https://doi.org/10.1021/nl901681d.

(7) Pinchetti, V.; Meinardi, F.; Camellini, A.; Sirigu, G.; Christodoulou, S.; Bae, W. K.; De Donato, F.; Manna, L.; Zavelani-Rossi, M.; Moreels, I.; Klimov, V. I.; Brovelli, S. Effect of Core/Shell Interface on Carrier Dynamics and Optical Gain Properties of Dual-Color Emitting CdSe/CdS Nanocrystals. *ACS Nano* **2016**, *10* (7), 6877–6887. https://doi.org/10.1021/acsnano.6b02635.

(8) Li, M.; Zhi, M.; Zhu, H.; Wu, W.-Y.; Xu, Q.-H.; Jhon, M. H.; Chan, Y. Ultralow-Threshold Multiphoton-Pumped Lasing from Colloidal Nanoplatelets in Solution. *Nat Commun* **2015**, *6* (1), 8513. https://doi.org/10.1038/ncomms9513.

(9) Yang, Z.; Pelton, M.; Fedin, I.; Talapin, D. V.; Waks, E. A Room Temperature Continuous-Wave Nanolaser Using Colloidal Quantum Wells. *Nat Commun* **2017**, *8* (1), 143. https://doi.org/10.1038/s41467-017-00198-z.

(10) Isik, F.; Delikanli, S.; Durmusoglu, E. G.; Isik, A. T.; Shabani, F.; Baruj, H. D.; Demir, H. V. "Giant" Colloidal Quantum Well Heterostructures of CdSe@CdS Core@Shell Nanoplatelets from 9.5 to 17.5 Monolayers in Thickness Enabling Ultra-High Gain Lasing. *Small* **2024**, *20* (38), 2309494. https://doi.org/10.1002/smll.202309494.
(11) Cassidy, J.; Diroll, B. T.; Mondal, N.; Berkinsky, D. B.; Zhao, K.; Harankahage, D.; Porotnikov, D.; Gately, R.; Khon, D.; Proppe, A.; Bawendi, M. G.; Schaller, R. D.; Malko, A. V.; Zamkov, M. Quantum Shells Boost the Optical Gain of Lasing Media. *ACS Nano* **2022**, *16* (2), 3017–3026. https://doi.org/10.1021/acsnano.1c10404.
(12) Zhao, K.; Zhou, X.; Li, X.; Moon, J.; Cassidy, J.; Harankahage, D.; Hu, Z.; Savoy, S. M.; Gu, Q.; Zamkov, M.; Malko, A. V. Green Light from Red-Emitting Nanocrystals: Broadband, Low-Threshold Lasing from Colloidal Quantum Shells in Optical Nanocavities. *ACS Nano* **2024**, *18* (16), 10946–10953. https://doi.org/10.1021/acsnano.4c02346.
(13) Ahn, N.; Livache, C.; Pinchetti, V.; Jung, H.; Jin, H.; Hahm, D.; Park, Y.-S.; Klimov, V. I. Electrically Driven Amplified Spontaneous Emission from Colloidal Quantum Dots. *Nature* **2023**, *617* (7959), 79–85. https://doi.org/10.1038/s41586-023-05855-6.
(14) Dang, C.; Lee, J.; Breen, C.; Steckel, J. S.; Coe-Sullivan, S.; Nurmikko, A. Red, Green and Blue Lasing Enabled by Single-Exciton Gain in Colloidal Quantum Dot Films. *Nature Nanotech* **2012**, *7* (5), 335–339. https://doi.org/10.1038/nnano.2012.61.
(15) Wang, C.; Wehrenberg, B. L.; Woo, C. Y.; Guyot-Sionnest, P. Light Emission and Amplification in Charged CdSe Quantum Dots. *J. Phys. Chem. B* **2004**, *108* (26), 9027–9031. https://doi.org/10.1021/jp0489830.
(16) Kozlov, O. V.; Park, Y.-S.; Roh, J.; Fedin, I.; Nakotte, T.; Klimov, V. I. Sub–Single-Exciton Lasing Using Charged Quantum Dots Coupled to a Distributed Feedback Cavity. *Science* **2019**, *365* (6454), 672–675. https://doi.org/10.1126/science.aax3489.
(17) Taghipour, N.; Dalmases, M.; Whitworth, G. L.; Dosil, M.; Othonos, A.; Christodoulou, S.; Liga, S. M.; Konstantatos, G. Colloidal Quantum Dot Infrared Lasers Featuring Sub-Single-Exciton Threshold and Very High Gain. *Advanced Materials* **2023**, *35* (1), 2207678. https://doi.org/10.1002/adma.202207678.
(18) Ivanov, S. A.; Nanda, J.; Piryatinski, A.; Achermann, M.; Balet, L. P.; Bezel, I. V.; Anikeeva, P. O.; Tretiak, S.; Klimov, V. I. Light Amplification Using Inverted Core/Shell Nanocrystals: Towards Lasing in the Single-Exciton Regime. *J. Phys. Chem. B* **2004**, *108* (30), 10625–10630. https://doi.org/10.1021/jp0483371.
(19) Nanda, J.; Ivanov, S. A.; Achermann, M.; Bezel, I.; Piryatinski, A.; Klimov, V. I. Light Amplification in the Single-Exciton Regime Using Exciton−Exciton Repulsion in Type-II Nanocrystal Quantum Dots. *J. Phys. Chem. C* **2007**, *111* (42), 15382–15390. https://doi.org/10.1021/jp0738659.
(20) Mahler, B.; Spinicelli, P.; Buil, S.; Quelin, X.; Hermier, J.-P.; Dubertret, B. Towards Non-Blinking Colloidal Quantum Dots. *Nat Mater* **2008**, *7* (8), 659–664. https://doi.org/10.1038/nmat2222.
(21) Spinicelli, P.; Buil, S.; Quélin, X.; Mahler, B.; Dubertret, B.; Hermier, J.-P. Bright and Grey States in CdSe-CdS Nanocrystals Exhibiting Strongly Reduced Blinking. *Phys. Rev. Lett.* **2009**, *102* (13), 136801. https://doi.org/10.1103/PhysRevLett.102.136801.
(22) Chen, Y.; Vela, J.; Htoon, H.; Casson, J. L.; Werder, D. J.; Bussian, D. A.; Klimov, V. I.; Hollingsworth, J. A. "Giant" Multishell CdSe Nanocrystal Quantum Dots with Suppressed Blinking. *J. Am. Chem. Soc.* **2008**, *130* (15), 5026–5027. https://doi.org/10.1021/ja711379k.
(23) Chen, O.; Zhao, J.; Chauhan, V. P.; Cui, J.; Wong, C.; Harris, D. K.; Wei, H.; Han, H.-S.; Fukumura, D.; Jain, R. K.; Bawendi, M. G. Compact High-Quality CdSe–CdS Core–Shell Nanocrystals with Narrow Emission Linewidths and Suppressed Blinking. *Nature Mater* **2013**, *12* (5), 445–451. https://doi.org/10.1038/nmat3539.

(24) Razgoniaeva, N.; Moroz, P.; Yang, M.; Budkina, D. S.; Eckard, H.; Augspurger, M.; Khon, D.; Tarnovsky, A. N.; Zamkov, M. One-Dimensional Carrier Confinement in "Giant" CdS/CdSe Excitonic Nanoshells. *J. Am. Chem. Soc.* **2017**, *139* (23), 7815–7822. https://doi.org/10.1021/jacs.7b02054.
(25) Diroll, B. T.; Cassidy, J. P.; Harankahage, D.; Hua, M.; Lin, X.-M.; Zamkov, M. Large Two-Photon Cross Sections and Low-Threshold Multiphoton Lasing of CdS/CdSe/CdS Quantum Shells. *Nanoscale* **2023**, *15* (45), 18415–18422. https://doi.org/10.1039/D3NR04203K.
(26) Tanghe, I.; Molkens, K.; Vandekerckhove, T.; Respekta, D.; Waters, A.; Huang, J.; Beavon, J.; Harankahage, D.; Lin, C. Y.; Chen, K.; Van Thourhout, D.; Zamkov, M.; Geiregat, P. Two-Dimensional Electron–Hole Plasma in Colloidal Quantum Shells Enables Integrated Lasing Continuously Tunable in the Red Spectrum. *ACS Nano* **2024**, *18* (22), 14661–14671. https://doi.org/10.1021/acsnano.4c02907.
(27) Wu, M.; Ha, S. T.; Shendre, S.; Durmusoglu, E. G.; Koh, W.-K.; Abujetas, D. R.; Sánchez-Gil, J. A.; Paniagua-Domínguez, R.; Demir, H. V.; Kuznetsov, A. I. Room-Temperature Lasing in Colloidal Nanoplatelets via Mie-Resonant Bound States in the Continuum. *Nano Lett.* **2020**, *20* (8), 6005–6011. https://doi.org/10.1021/acs.nanolett.0c01975.
(28) Kersuzan, C.; Celaj, S.; Daney de Marcillac, W.; Pons, T.; Maître, A. Photolithographed Whispering Gallery Mode Microdisk Cavities Coupled to Semiconductor Quantum Dots. *ACS Photonics* **2024**, *11* (4), 1715–1723. https://doi.org/10.1021/acsphotonics.4c00023.
(29) Ouyang, X.; Liu, T.; Zhang, Y.; He, J.; He, Z.; Zhang, A. P.; Tam, H.-Y. Ultrasensitive Optofluidic Enzyme-Linked Immunosorbent Assay by on-Chip Integrated Polymer Whispering-Gallery-Mode Microlaser Sensors. *Lab Chip* **2020**, *20* (14), 2438–2446. https://doi.org/10.1039/D0LC00240B.
(30) Chiasera, A.; Dumeige, Y.; Féron, P.; Ferrari, M.; Jestin, Y.; Nunzi Conti, G.; Pelli, S.; Soria, S.; Righini, G. C. Spherical Whispering-Gallery-Mode Microresonators. *Laser & Photon. Rev.* **2010**, *4* (3), 457–482. https://doi.org/10.1002/lpor.200910016.
(31) Liptay, T. J.; Marshall, L. F.; Rao, P. S.; Ram, R. J.; Bawendi, M. G. Anomalous Stokes Shift in CdSe Nanocrystals. *Phys. Rev. B* **2007**, *76* (15), 155314. https://doi.org/10.1103/PhysRevB.76.155314.
(32) Brovelli, S.; Schaller, R. D.; Crooker, S. A.; García-Santamaría, F.; Chen, Y.; Viswanatha, R.; Hollingsworth, J. A.; Htoon, H.; Klimov, V. I. Nano-Engineered Electron–Hole Exchange Interaction Controls Exciton Dynamics in Core–Shell Semiconductor Nanocrystals. *Nat Commun* **2011**, *2* (1), 280. https://doi.org/10.1038/ncomms1281.
(33) Cui, J.; Beyler, A. P.; Marshall, L. F.; Chen, O.; Harris, D. K.; Wanger, D. D.; Brokmann, X.; Bawendi, M. G. Direct Probe of Spectral Inhomogeneity Reveals Synthetic Tunability of Single-Nanocrystal Spectral Linewidths. *Nature Chem* **2013**, *5* (7), 602–606. https://doi.org/10.1038/nchem.1654.
(34) Cui, J.; Beyler, A. P.; Coropceanu, I.; Cleary, L.; Avila, T. R.; Chen, Y.; Cordero, J. M.; Heathcote, S. L.; Harris, D. K.; Chen, O.; Cao, J.; Bawendi, M. G. Evolution of the Single-Nanocrystal Photoluminescence Linewidth with Size and Shell: Implications for Exciton–Phonon Coupling and the Optimization of Spectral Linewidths. *Nano Lett.* **2016**, *16* (1), 289–296. https://doi.org/10.1021/acs.nanolett.5b03790.
(35) Li, Q.; Lian, T. Exciton Spatial Coherence and Optical Gain in Colloidal Two-Dimensional Cadmium Chalcogenide Nanoplatelets. *Acc. Chem. Res.* **2019**, *52* (9), 2684–2693. https://doi.org/10.1021/acs.accounts.9b00252.
(36) Mohamed, M. B.; Tonti, D.; Al-Salman, A.; Chemseddine, A.; Chergui, M. Synthesis of High Quality Zinc Blende CdSe Nanocrystals. *J. Phys. Chem. B* **2005**, *109* (21), 10533–10537. https://doi.org/10.1021/jp051123e.
(37) Rossinelli, A. A.; Riedinger, A.; Marqués-Gallego, P.; Knüsel, P. N.; Antolinez, F. V.; Norris, D. J. High-Temperature Growth of Thick-Shell CdSe/CdS Core/Shell Nanoplatelets. *Chem. Commun.* **2017**, *53* (71), 9938–9941. https://doi.org/10.1039/C7CC04503D.

(38) Rossinelli, A. A.; Rojo, H.; Mule, A. S.; Aellen, M.; Cocina, A.; De Leo, E.; Schäublin, R.; Norris, D. J. Compositional Grading for Efficient and Narrowband Emission in CdSe-Based Core/Shell Nanoplatelets. *Chem. Mater.* **2019**, *31* (22), 9567–9578. https://doi.org/10.1021/acs.chemmater.9b04220.